INORGANIC CHEMISTRY
FRONTIERS

RESEARCH ARTICLE

View Article Online
View Journal | View Issue

Cite this: *Inorg. Chem. Front.*, 2019, **6**, 765

Boosting photochemical activity by Ni doping of mesoporous CoO nanoparticle assemblies†

Georgia Velegraki,[a] Ioannis Vamvasakis,[a] Ioannis T. Papadas,[b] Sotiris Tsatsos,[c] Anastasia Pournara,[d] Manolis J. Manos,[d] Stelios A. Choulis,[c] Stella Kennou,[c] Georgios Kopidakis[a] and Gerasimos S. Armatas *[a]

Received 9th December 2018,
Accepted 3rd February 2019

DOI: 10.1039/c8qi01324a

rsc.li/frontiers-inorganic

The rational design of semiconductor nanostructures is of utmost importance for efficient solar energy conversion and environmental remediation. In this article, we report high-surface-area mesoporous networks consisting of Ni-implanted cubic CoO ($Co_{1-x}Ni_xO$) nanoparticles as promising catalysts for the detoxification of aqueous Cr(VI) solutions. Mechanistic studies with X-ray photoelectron, UV–vis optical absorption, fluorescence and electrochemical impedance spectroscopy and theoretical (DFT) calculations indicate that the performance enhancement of these catalysts arises from the high charge transfer kinetics and oxidation efficiency of surface-reaching holes. By tuning the chemical composition, the $Co_{1-x}Ni_xO$ mesoporous catalyst at 2 atomic% Ni content imparts outstanding photocatalytic Cr(VI) reduction and water oxidation activity, corresponding to an apparent quantum yield (QY) of 1.5% at λ = 375 nm irradiation light.

1. Introduction

Hexavalent chromium (Cr(VI)) constitutes a serious chemical residue in wastewater arising from various industrial activities, such as electroplating, leather tanning and paint manufacturing among others. Contamination by Cr(VI) species results in groundwater pollution with devastating effects on the environment.[1] In particular, Cr(VI) is a non-biodegradable contaminant that is responsible for human carcinogens and mutagens according to the International Agency for Research on Cancer (IARC), classifying it as a Group 1 carcinogen with a lethal dose (LD50) of 50–150 mg kg^{-1} for an adult.[2] Therefore, neutralization of Cr(VI)-bearing solutions is of utmost importance in terms of protecting the environment and human health.

Recently, the research community has strived for the remediation of Cr(VI) ions through the photocatalytic reduction method, that is, reduction of Cr(VI) to less harmful Cr(III), which can be precipitated as $Cr(OH)_3$ or Cr_2O_3 in alkaline solutions.[3] To this end, various semiconductor materials, such as TiO_2, ZnO, WO_3, SnS_2, Bi_2S_3 and CdS, have been investigated as catalysts for Cr(VI) photoreduction.[4] Nevertheless, although promising, these materials suffer from low solar energy absorption, short lifetime of photogenerated electron–hole pairs and poor electrical conductivity, which adversely impact their viability for use in photocatalysis. Furthermore, most of these catalysts operate in the presence of a hole scavenger such as ascorbic acid, citric acid and ethylenediamine-tetraacetic acid (EDTA), which seriously impedes their utilization in Cr(VI)-rich wastewaters. Therefore, devising cost-effective catalysts for detoxification of Cr(VI)-contaminated aquatic systems is an ongoing research challenge.

Cobalt monoxide (CoO) has recently emerged as an attractive material for redox catalysis, gas sensor devices and lithium-ion batteries due to its high redox activity, visible light response (band gap (E_g) ~2.2–2.8 eV) and chemical stability.[5] CoO crystallizes in a cubic rock-salt and hexagonal wurtzite structure. Generally, the cubic close-packed structure of CoO is thermodynamically more stable than the hexagonal ones but suffers from poor catalytic activity.[6] Catalytic systems of cubic CoO have only recently demonstrated promising activity for CO oxidation and photocatalytic water-splitting reactions.[7]

Herein, we report for the first time chemically stable and robust mesoporous networks of Ni-implanted cubic CoO nanoparticles (NPs) that present high photocatalytic activity for Cr(VI) reduction and water oxidation under UV and visible light irradiation. We utilize a polymer-assisted self-assembly of colloidal NPs to assemble mesoporous $Co_{1-x}Ni_xO$ (x = 0–0.05) NP-linked frameworks with high interstitial porosity. This

[a]*University of Crete, Department of Materials Science and Technology, Heraklion 71003, Greece. E-mail: garmatas@materials.uoc.gr*
[b]*Cyprus University of Technology, Department of Mechanical Engineering and Materials Science and Engineering, Limassol 3041, Cyprus*
[c]*University of Patras, Department of Chemical Engineering, Patra 26504, Greece*
[d]*University of Ioannina, Department of Chemistry, Ioannina 45110, Greece*

†Electronic supplementary information (ESI) available: Electrochemical data, TGA profile, TEM images, XRD patterns, N_2 physisorption isotherms, XPS spectra, FL spectra and catalytic data of $Co_{1-x}Ni_xO$ MNAs. See DOI: 10.1039/c8qi01324a

method utilizes the NPs as building block units and is based on the coassembly of these nanoscopic particles with organic structure-directing agents to construct three-dimensional structures with open-pore morphology.[8] The resulting materials, unlike individual NPs and bulk microstructures, feature a nanometer-sized framework perforated by uniform pores, which allows rapid mass transport and provides plenty of exposed surface-active sites available for reaction. Moreover, we highlight the effect of the Ni dopant on the electronic structure and photochemical performance of CoO by using a combination of experiment and theoretical methods. The results of this study can offer new insights into the design and development of efficient photocatalysts for environmental remediation and energy conversion applications.

2. Results and discussion

2.1 Synthesis and structural analysis of mesoporous $Co_{1-x}Ni_xO$ assemblies

The synthesis of mesoporous assemblies from colloidal $Co_{1-x}Ni_xO$ NPs (denoted as $Co_{1-x}Ni_xO$ MNAs, x = 0, 0.01, 0.02 and 0.05) was accomplished by a polymer-templated self-assembly method. In short, a poly(ethylene oxide)-*b*-poly(propylene oxide)-*b*-poly(ethylene oxide) block copolymer was utilized to template the aggregating self-assembly of BF_4^--stabilized $Co_{1-x}Ni_xO$ NPs in a mixed *N*,*N*-dimethyloformamide (DMF)/tetrahydrofuran (THF) solution. The reaction mixture was kept under stirring for 2 h approximately, followed by slow evaporation of the solvent (within 5–6 days) at 40 °C in order for mesostructured NP/polymer composites to be formed. Finally, the polymer template was removed by decomposition at 350 °C to give a continuous network of connected NPs with a large internal surface area (details are given in the Experimental section). The elimination of the organic phase upon heating was confirmed by thermogravimetric analysis (TGA), see Fig. S1 and S2.† The Ni composition in implanted samples was determined by energy dispersive X-ray spectroscopy (EDS) and anodic stripping voltammetry (ASV). Results showed that the molar ratio Ni/Co in the samples was very close to the expected composition from the stoichiometry of reactions (Table 1).

Table 1 Analytical data and textural properties of mesoporous $Co_{1-x}Ni_xO$ MNAs

Sample	Ni content[a] (atomic%) EDS	ASV	Surface area ($m^2\ g^{-1}$)	Pore volume ($cm^3\ g^{-1}$)	Pore size (nm)
CoO MNAs			137	0.15	4.4
$Co_{0.99}Ni_{0.01}O$	0.99	1.09 ± 0.14	108	0.16	4.3
$Co_{0.98}Ni_{0.02}O$	1.89	2.06 ± 0.07	112	0.16	4.5
$Co_{0.95}Ni_{0.05}O$	4.81	4.97 ± 0.44	115	0.15	4.4

[a] Ni/(Co + Ni) atomic ratio based on EDS and anodic stripping voltammetry (ASV) analysis.

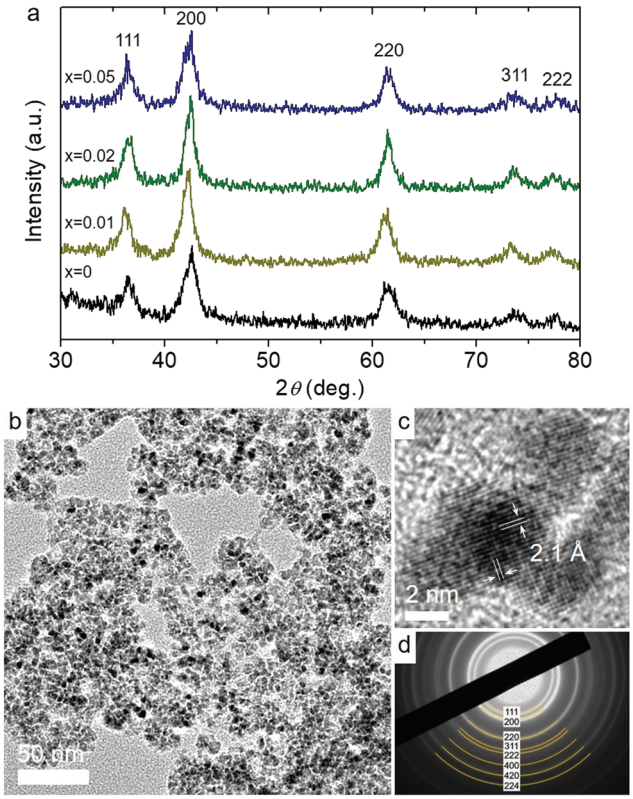

Fig. 1 (a) XRD patterns of $Co_{1-x}Ni_xO$ MNAs. (b) Typical TEM image, (c) high-resolution TEM, showing the lattice fringes of CoO along the [001] direction, and (d) SAED pattern of $Co_{0.98}Ni_{0.02}O$ MNAs.

X-ray diffraction (XRD) measurements were performed to investigate the crystal structure of the as-prepared materials. In Fig. 1a, all samples exhibit broad but distinct XRD peaks that correspond to the cubic rock-salt structure of CoO with *Fm*3*m* symmetry (JCPDS no 48-1719). No impurity peaks corresponding to other chemical phases of cobalt like Co_3O_4 were detected, indicating the phase purity of the materials. However, due to the low concentration of Ni in $Co_{1-x}Ni_xO$ MNAs, no corresponding XRD peaks can be observed. Using the peak width of the (200) diffraction and Scherrer's equation, the crystallite size of the mesoporous materials was estimated to be ~6.5–7 nm, which is very close to the grain size of the precursor NPs (data not shown).

Fig. 1b and Fig. S3a† display typical transmission electron microscopy (TEM) images obtained from mesoporous assemblies of CoO and $Co_{0.98}Ni_{0.02}O$ NPs; $Co_{0.98}Ni_{0.02}O$ MNAs are the most active catalyst among the studied materials. The images show a porous network of connected NPs with an average size of *ca.* 5–6 nm, which is very close to the crystallite sizes obtained from XRD, implying minimal grain coarsening of NPs during synthesis. Crystal structure features of CoO and $Co_{0.98}Ni_{0.02}O$ MNAs were also characterized by high-resolution TEM (HRTEM) and selected-area electron diffraction (SAED). The HRTEM images shown in Fig. 1c and the inset of Fig. S3a† suggest single-crystalline NPs, showing distinct lattice fringes throughout the entire particles with ~2.1 Å inter-

layer distances that correspond to the (200) crystallographic planes of cubic CoO. Besides, the SAED patterns in Fig. 1d and Fig. S3b† signify the polycrystalline nature of the porous frameworks, displaying a series of Debye-Scherrer rings. In agreement with XRD results, all the diffraction rings can be assigned to the cubic phase of CoO.

Nitrogen physisorption experiments corroborate that $Co_{1-x}Ni_xO$ MNAs contain mesopores within the assembled structure. All samples showed type-IV adsorption–desorption isotherms with a H_3 type hysteresis loop at high relative pressures (Fig. S4†), which are characteristic of mesoporous solids with slit-like pores.[9] The specific surface areas, which were derived using the Brunauer–Emmett–Teller (BET) method on the absorption data, and the total pore volumes of the Ni-implanted samples were found to be 108–115 $m^2\ g^{-1}$ and 0.15–0.16 $cm^3\ g^{-1}$, respectively, which are comparable to those of pure CoO MNAs (137 $m^2\ g^{-1}$ and 0.15 $cm^3\ g^{-1}$, respectively). The slightly lower surface area of the Ni-doped samples relative to the unmodified CoO MNAs could be attributed to the close packing of the $Co_{1-x}Ni_xO$ NPs which form a more dense (crack-free) pore wall, although the slightly higher mass density of the NiO_x phase (6.67 g cm^{-3}) compared to that of CoO (6.44 g cm^{-3}) is a possible explanation. Analysis of the adsorption data using the non-local density functional theory (NLDFT) method revealed a narrow size distribution of pores with the pore diameter being in the range of 4.3–4.5 nm. All the analytical and textural properties of $Co_{1-x}Ni_xO$ MNAs are listed in Table 1.

The surface chemical state of pristine CoO and $Co_{0.98}Ni_{0.02}O$ MNA materials was examined by X-ray photoelectron spectroscopy (XPS). For the CoO MNA catalyst, the Co $2p_{3/2}$ XPS core-level peak is detected at a binding energy of 781.1 eV with a shake-up satellite feature at about 786.4 eV, providing convincing evidence of the existence of Co(II) ions (Fig. 2a).[10] The Co $2p_{3/2}$ signal is clearly observed at slightly lower binding energies (780.8 eV) for the $Co_{0.98}Ni_{0.02}O$ MNAs, possibly due to a partial electron transfer from Ni to Co through the bridging oxygen atoms.[11] Specifically, the single occupied 3d t_{2g} orbital of high-spin Co(II) ($t_{2g}^5e_g^2$ electron configuration) can interact with the oxygen lone pairs, accepting electrons *via* π-donation. After Ni doping, the fully occupied 3d t_{2g} states of Ni(II) ($t_{2g}^6e_g^2$ electron configuration) can strengthen the partial electron transfer from oxygen to Co(II) due to the repulsive interactions with the occupied 2p orbitals of oxygen.[12] In agreement with this, the O 1s XPS spectrum of $Co_{0.98}Ni_{0.02}O$ MNAs, which is deconvoluted into two peaks assigned to the lattice oxygen (530.0 eV) and the hydroxyl groups (532.0 eV), is slightly red-shifted compared to that of CoO (530.3 eV and 532.2 eV), Fig. 2b. This downshift in binding energies (by ~0.2–0.3 eV) for oxygen atoms is thought to be related to the incorporation of Ni. Comparatively, the O 1s spectrum of the polycrystalline NiO sample shows two distinct peaks at 529.4 eV and 531.2 eV (Fig. S5†). Since the Ni content in $Co_{0.98}Ni_{0.02}O$ MNAs is as low as 1.56 wt%, it is difficult to directly detect by XPS (the XPS Ni $2p_{3/2}$ peak is typically observed in the range of 854.2–854.5 eV). In line with XPS results, the valence band (VB) spectra of CoO and $Co_{0.98}Ni_{0.02}O$ MNAs provide an additional hint for the incorporation of Ni into the CoO lattice (Fig. 2c). The CoO shows a photoemission onset, which is defined as the energetic difference between the Fermi energy and the VB edge, at *ca.* 0.31 eV, indicating a p-type character. For the $Co_{0.98}Ni_{0.02}O$ MNAs, the photoemission onset is shifted to *ca.* 0.26 eV, reflecting a downshift of the Fermi level due to the Ni doping. Consistent with this interpretation, the photoelectron emission onset of polycrystalline NiO was found at 0.22 eV.

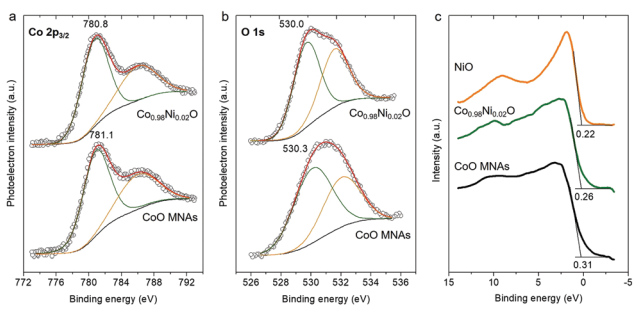

Fig. 2 XPS spectra of the (a) Co $2p_{3/2}$, (b) O 1s and (c) valence band region of CoO and $Co_{0.98}Ni_{0.02}O$ MNAs. In panel (c), the XPS valence band spectrum of polycrystalline NiO is also given.

2.2 Photocatalytic Cr(VI) reduction activity

The catalytic activity of the title materials was investigated in photoreduction of aqueous Cr(VI) solutions under λ >360 nm light irradiation. Fig. 3a depicts the evolution of Cr(VI) reduction over $Co_{1-x}Ni_xO$ MNA catalysts with different Ni loadings (from 0 to 5 atomic%). The comparison shows that $Co_{0.98}Ni_{0.02}O$ MNAs exhibit better performance for Cr(VI) photoreduction, achieving ~90% Cr(VI) conversion in 4 h, which is markedly higher than that of pure CoO MNAs (~46% Cr(VI) conversion level, 4 h). The outstanding photocatalytic performance of $Co_{0.98}Ni_{0.02}O$ MNAs is also evident from their high apparent quantum yield (QY ~1.5% at 375 nm and ~0.8% at 410 nm), which is comparable or even higher to that of other highly active catalysts, such as hexagonal CoO NP assemblies (~1.61% at 375 nm),[13] Au/TiO_2-Pt (~1.0% at 550 nm),[14] $CuFe_2O_4$/CdS (~1.1% at 430 nm)[15] and $CuAl_2O_4$/TiO_2 (~0.11% under white light)[16] composites. Of note, the optimum catalyst dosage was found to be 0.3 g L^{-1} by performing a series of photocatalytic Cr(VI) reduction tests with different catalyst concentrations (from 0.2 to 0.4 g L^{-1}, see Fig. S6†). Moreover, because of the visible light absorption of $Co_{1-x}Ni_xO$ NPs (E_g ~2.5–2.7 eV, as estimated by optical absorption spectra, see the inset of Fig. 5), $Co_{1-x}Ni_xO$ MNAs can also carry out photocatalytic Cr(VI) reduction with reasonable activity under λ >420 nm irradiation. As shown in Fig. 3a, ~27% and ~50% Cr(VI) conversion yield was obtained with visible-light irradiated CoO and $Co_{0.98}Ni_{0.02}O$ MNA dispersions in 4 h, respectively.

In addition to the chemical composition, morphological effects may also contribute to the high photocatalytic activity of $Co_{1-x}Ni_xO$ MNAs. As a proof of concept, we investigated the

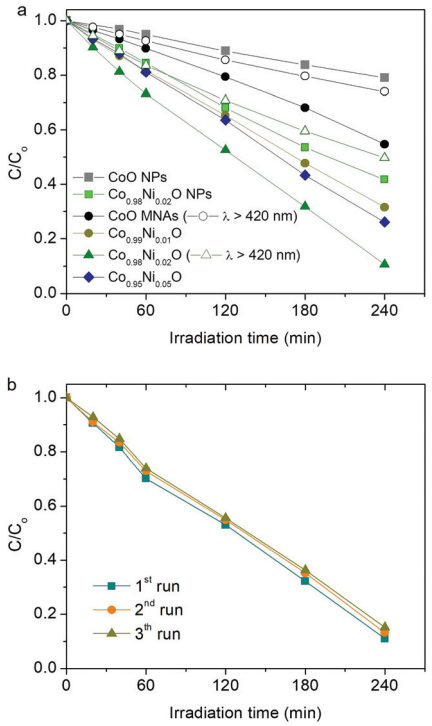

Fig. 3 (a) Photocatalytic reduction of aqueous Cr(VI) with $Co_{1-x}Ni_xO$ MNAs catalysts. The photocatalytic activity of isolated CoO and $Co_{0.98}Ni_{0.02}O$ NPs under λ >360 nm light and CoO and $Co_{0.98}Ni_{0.02}O$ MNA catalysts under λ >420 nm light irradiation is also given. (b) Recycling study of $Co_{0.98}Ni_{0.02}O$ MNAs. Reaction conditions: 0.3 g L^{-1} catalyst, 50 mg L^{-1} Cr(VI) solution, pH = 2, λ >360 nm light, 20 °C.

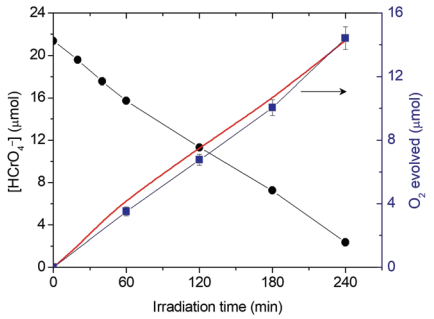

Fig. 4 Comparison of photocatalytic Cr(VI) reduction (black) and oxygen evolution (experimental: blue line, calculated from the $HCrO_4^-$ concentration-time data and stoichiometry of reaction (1): red line) as a function of irradiation time for the $Co_{0.98}Ni_{0.02}O$ MNA catalyst under λ >360 nm light irradiation (Reaction conditions: 0.3 g L^{-1} catalyst, 50 mg L^{-1} Cr(VI) solution, λ >360 nm light, pH = 2, 20 °C).

photocatalytic Cr(VI) reduction activity of isolated (BF_4^--capped) CoO and $Co_{0.98}Ni_{0.02}O$ NPs under identical conditions and the results are depicted in Fig. 3a. It can be seen that individual CoO and $Co_{0.98}Ni_{0.02}O$ NPs afforded a considerably lower catalytic activity (*ca.* 21% and 58% Cr(VI) conversion level in 4 h, respectively) than that obtained for Cr(VI) photoreduction over the corresponding mesoporous NP assemblies. These results clearly indicate that the material's open-pore structure and accessible surface area play an important role in the reduction rate of Cr(VI).

The $Co_{0.98}Ni_{0.02}O$ MNA catalyst also demonstrates very good stability over a period of 12 h. The reusability of the catalyst was assessed within three recycling experiments, in which the catalyst after each run was collected by centrifugation and re-dispersed in a fresh Cr(VI) aqueous solution. As shown in Fig. 3b, the $Co_{0.98}Ni_{0.02}O$ MNAs retain more than 94% of their initial activity after recycling. Moreover, XRD, N_2 porosimetry and XPS characterization of the reused sample indicated that its crystal structure, porous morphology and surface chemical state are well maintained after catalysis, substantiating high durability (see Fig. S7–S9†).

2.3 Effect of the Ni dopant on photochemical activity

To understand the oxidation mechanism over $Co_{1-x}Ni_xO$ assemblies, we carried out photoreduction of Cr(VI) (50 mg L^{-1}) in an air-tight quartz cell and the evolved oxygen gas was analyzed by gas chromatography. The results showed that $Co_{0.98}Ni_{0.02}O$ MNAs are effective at oxidizing water to dioxygen (Fig. 4), giving an average O_2 evolution rate of ~3.5 μmol h^{-1} after 4 h of irradiation. Moreover, to prove that the generation of oxygen is indeed a photoinduced effect, the evolved gas was monitored with an on-line gas analyzer. When light on and off conditions were applied to a $Co_{0.98}Ni_{0.02}O$ MNA dispersion (0.3 g L^{-1}) for photocatalytic Cr(VI) reduction, a transient O_2 evolution response was detected (Fig. S10†), suggesting that the present Cr(VI) photoreduction proceeds simultaneously with the water oxidation reaction. Thus, the overall reaction can be described by the following equation in which the hydrogen chromate ($HCrO_4^-$) ions are the predominating species in conditions with pH <6 and Cr(VI) concentrations <100 mg L^{-1}.[17]

$$2HCrO_4^- + 8H^+ \rightarrow 2Cr^{3+} + \frac{3}{2}O_2 + 5H_2O \quad (1)$$

It is noteworthy that the calculated oxygen evolution derived from eqn (1) matches well with the experimental results (Fig. 4). In particular, we obtained a $HCrO_4^-$ reduction rate of about 5.2 μmol h^{-1} which, based on eqn (1), consists of a ~3.9 μmol h^{-1} O_2 evolution rate. These results prove that, under UV–visible irradiation, a prominent fraction of surface-reaching holes is associated with the water oxidation reaction to produce oxygen.

Apart from the oxygen evolution, photooxidation of surface hydroxyl (–OH) groups to hydroxyl radicals ($^{\bullet}OH$) is a possible option. Recently, we have demonstrated that this is a viable process for hexagonal CoO catalysts in the photocatalytic reduction of Cr(VI).[13] To elucidate this possibility, we resort to the fluorescence (FL) study of the Cr(VI) photoreduction over pure and Ni-doped CoO (2% Ni loading) MNAs in the presence of coumarin as a fluorophore; coumarin reacts with hydroxyl radicals to produce fluorescence umbelliferone. The time evolution of the FL emission of umbelliferone reveals that the production rate of $^{\bullet}OH$ radicals, defined as the ratio of the intensity of umbelliferone to the intensity of coumarin, is

comparable between these two materials (see Fig. S11†). Also, the FL signal of umbelliferone does not show an obvious intensity increase after 1 h of illumination. Therefore, it is reasonable to conclude that the observed OH_{aq}^- oxidation process for both pure and Ni-doped CoO MNA catalysts is minimal and, instead, the oxidation product is almost exclusively O_2. This is consistent with the O_2 evolution data shown in Fig. 4.

The above catalytic results clearly suggest that the four-electron water oxidation process ($2H_2O \rightarrow O_2 + 4H^+ + 4e^-$) at the $Co_{1-x}Ni_xO$ surface dictates the overall reaction rate. As a proof of concept, the Cr(VI) reduction activity of $Co_{0.98}Ni_{0.02}O$ MNAs is also investigated in the presence of phenol, citric acid and EDTA as sacrificial electron donors. Since oxidation of these organic compounds is thermodynamically and kinetically more favorable than water oxidation (E_{ox} for phenol, citric acid, EDTA and water is 0.97 V, 1.2 V, 1.17 V and 0.82 V *vs.* NHE (pH 7), respectively),[18] it is anticipated that this process will enhance the kinetics of the Cr(VI) reduction. As expected, the Cr(VI) degradation is significantly accelerated with the addition of 1 equiv. of the above sacrificial reagents, resulting in complete conversion of Cr(VI) in 3–3.5 h (Fig. S12a†). Assuming that the reaction rate is proportional to the Cr(VI) concentration, the photocatalytic reaction can be described by the first-order kinetics of the Langmuir–Hinshelwood model: $\ln(C/C_0) = -kt$, where C_0 and C are the concentration of Cr(VI) at initial time and time t, respectively, and k is the apparent reaction rate constant. Thus, kinetic analysis of the temporal evolution of the Cr(VI) concentration reveals that photoreduction proceeds at a rate (k) of 4.4×10^{-3} min^{-1}, 7.0×10^{-3} min^{-1} and 9.7×10^{-3} min^{-1} with phenol, citric acid and EDTA, respectively (Fig. S12b†). In comparison, an about two to six times lower reaction rate (1.7×10^{-3} min^{-1}) was observed without a sacrificial reagent, signifying that the presence of organic contaminants in the Cr(VI)-containing wastewater has an additive effect on improving the photocatalytic activity of $Co_{1-x}Ni_xO$ MNAs.

To elucidate the effect of the Ni dopant on the photocatalytic activity of CoO NPs, the electrochemical behavior of the as-prepared materials was delineated by electrochemical impedance spectroscopy (EIS). The Mott–Schottky plots ($1/C_{sc}^2$ *vs.* E) of the $Co_{1-x}Ni_xO$ MNA depositions onto a fluorine-doped tin oxide (FTO) substrate recorded in a 0.5 M Na_2SO_4 electrolyte (pH 7) are shown in Fig. 5. Using extrapolation to $1/C_{sc}^2 = 0$, the flat-band potentials (E_{FBs}) calculated for $Co_{1-x}Ni_xO$ MNAs were 1.15 ($x = 0$), 1.17 ($x = 0.01$), 1.20 ($x = 0.02$) and 1.22 ($x = 0.05$) V *versus* the normal hydrogen electrode (NHE). Consistent with VB XPS results, the negative slope of the $1/C_{sc}^2$–E curves confirms the p-type behavior of the catalysts. The anodic shift in E_{FB} for CoO upon Ni doping is due to the formation of Co–O–Ni linkages in implanted $Co_{1-x}Ni_xO$ samples. In fact, substitution of Co(II) with Ni(II) impurities can create localized Ni 3d states near the VB maximum, increasing the hole density in $Co_{1-x}Ni_xO$. The presence of these acceptor states will shift the Fermi level downward, improving the p-type conductivity of CoO, as suggested by VB

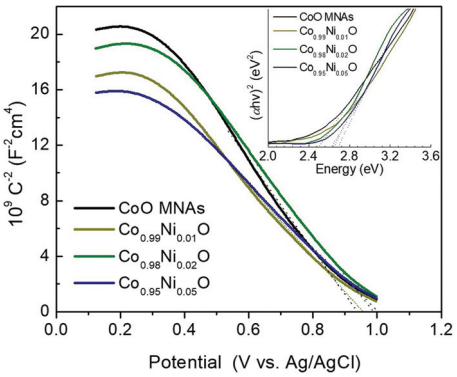

Fig. 5 Mott–Schottky plots (Inset: Tauc plots derived from UV–vis diffuse reflectance spectra) of the $Co_{1-x}Ni_xO$ MNA catalysts.

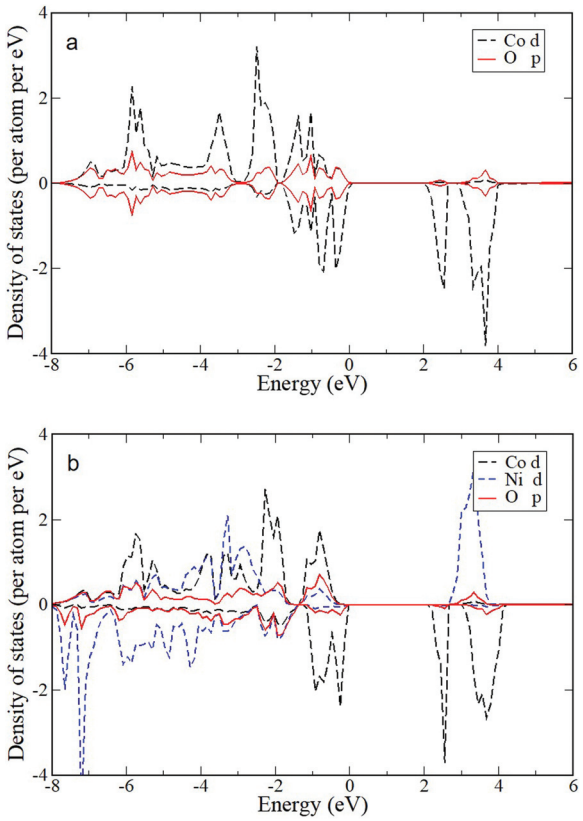

Fig. 6 Projected DOS for (a) CoO and (b) $Co_{0.5}Ni_{0.5}O$ rocksalt crystal structures. The DOS profiles near the Fermi level give an energy band gap of 2.0 and 2.1 eV for CoO and the $Co_{0.5}Ni_{0.5}O$ lattice, respectively.

XPS measurements and theoretical density functional theory (DFT+U) calculations. Electronic structure calculations show hybridization of O 2p and Co/Ni 3d states and direct transitions. The projected electronic density of states (DOS) for pure CoO in the rocksalt structure near the Fermi level (Fig. 6a) gives an electronic band gap of 2.0 eV (the quasi-particle bandgap value is higher and can be found with GW calculations that are beyond the scope of this work). In order

to examine the effects of doping on the electronic structure, Co atoms were replaced by Ni atoms in the CoO simulation cells. DFT+U calculations for $Co_{0.5}Ni_{0.5}O$ show that the separation between valence and conduction band edges increases by 0.1 eV and that there is strong mixing of the O 2p and Co/Ni 3d orbitals (Fig. 6b). These trends are also confirmed by calculations for smaller Ni concentrations with larger simulation cells ($Co_{0.75}Ni_{0.25}O$ and $Co_{0.9375}Ni_{0.0625}O$). Consistent with theoretical calculations, the carrier (acceptor) density (N_A) of $Co_{1-x}Ni_xO$ MNAs, as calculated by the slope of the $1/C_{sc}^2$–E plots, increases from 3.31×10^{16} to 4.57×10^{16} cm^{-3} with a higher level of nickel doping (Table S1†).

In Fig. 7a, the energy band diagram for each catalyst is illustrated. For heavily p-doped semiconductors such as CoO, it is quite reasonable to assume that the E_{FB} level lies very close to the VB edge. Thus, the position of the conduction band (CB) edge can be obtained by the equation $E_{CB} = E_{FB} + E_g$. UV–vis diffuse reflectance spectroscopy was used to obtain optical absorption spectra of $Co_{1-x}Ni_xO$ MNAs, from which the E_g values were estimated to be 2.50, 2.63, 2.66 and 2.69 eV for CoO and Ni-implanted samples with 1%, 2% and 5% Ni content, respectively (Table S1†), using Tauc plot analysis [$(Fhv)^2$ *versus* photon energy, where F, h, and v are the Kubelka–Munk function of the reflectance, Planck constant, and light frequency, respectively] (inset of Fig. 5). As shown in Fig. 7a, while a small perturbation of the CB edge is observed, the VB edge position of $Co_{1-x}Ni_xO$ MNAs shifts gradually to the anodic direction with increasing Ni doping, making them better electron acceptors for water oxidation, thus signifying superior Cr(VI) photoreduction kinetics.

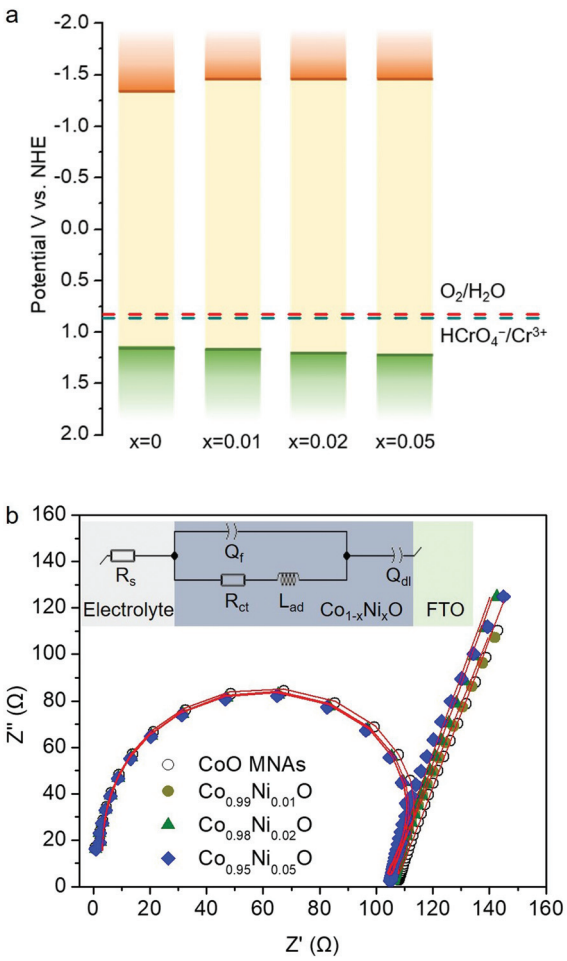

Fig. 7 (a) Energy band diagrams and (b) Nyquist plots of the $Co_{1-x}Ni_xO$ MNAs.

In addition, from EIS measurements and Nyquist Plots, we received information about the charge-transfer resistance (R_{ct}) for each catalyst (Fig. 7b). The EIS measurements were carried out in a conventional three-electrode cell containing 0.5 M KOH solution in the frequency range from 1 Hz to 1 MHz. An equivalent circuit model $R_s(Q_f/(R_{ct}L_{ad})Q_{dl})$ (see the inset of Fig. 7b) was used to simulate the EIS curve of the fabricated $Co_{1-x}Ni_xO$ MNA electrodes. In this circuit model, R_s represents the electrolyte resistance, R_{ct} is the charge-transfer resistance, and Q_f and Q_{dl} elements account for the defect resistance (pores, cracks and grain boundaries) of the solid film and the double layer capacitance, respectively. In addition, an inductor (L_{ad}), regarding the pseudo-inductive behaviour observed in the high frequency domain (often caused by disordered charge-carrier relaxation and disordered movement of redox species at the surface of electrode),[19] was also necessary for fitting the experimental results. Apparently, results of this study revealed that Ni-doped samples possess a lower R_{ct} than pure CoO MNAs does, affirming better charge carrier conductivity, which correlates well with their high Cr(VI) photoreduction activity. In particular, a R_{ct} value of 103.8, 100.7, 100.5 and 99.8 Ω is obtained for pure and 1%, 2% and 5% Ni implanted CoO MNAs (Table S2†). In fact, a lower R_{ct} value is anticipated to enhance the photoactivity of the catalyst by facilitating faster transport of charge carriers within the framework and prolonging the lifetime of photogenerated electron–hole pairs. Therefore, compared with CoO MNAs, the higher performance of Ni-doped samples can be attributed to the enhanced charge transfer and oxidative ability of surface-reaching holes. In line with this, the $Co_{0.98}Ni_{0.02}O$ MNA catalyst exhibits higher mobility of the photogenerated carriers according to the photocurrent density (J_{ph}) measurements; the J_{ph} for $Co_{1-x}Ni_xO$ MNAs was found to be 9.52 (x = 0), 11.01 (x = 0.01), 19.89 (x = 0.02) and 14.36 (x = 0.05) mA cm^{-2} under 420–760 nm irradiation at 1 V applied bias (see details in the Experimental section). Thus, the improved photochemical properties of $Co_{0.98}Ni_{0.02}O$ MNAs can be interpreted as a result of the high p-type conductivity and efficient dissociation of excitons into spatially separated electron–hole pairs.

3. Conclusions

In summary, high-surface-area Ni-doped CoO NP assemblies have been successfully prepared by a polymer-assisted self-assembly method, and then used as photocatalysts for the detoxification of Cr(VI) aqueous solutions. Significantly, the

$Co_{1-x}Ni_xO$ MNA catalyst at 2 atomic% Ni content achieves higher Cr(VI) photoreduction and water oxidation activity (>90% Cr(VI) conversion and ~3.5 μmol h^{-1} O_2 evolution rate after 4 h of irradiation) with 1.5% apparent QY at 375 nm, while demonstrating very good stability, outperforming previous results. Mechanistic studies with X-ray photoelectron, UV–vis optical absorption, fluorescence and electrochemical impedance spectroscopy experiments and theoretical (DFT) calculations reveal that Ni doping of CoO causes a gradual shift of the VB edge position to the anodic direction and enhancement of the p-type conductivity of CoO. These electronic characteristics effectively improve the charge-transfer process and oxidation efficiency of surface-reaching holes for water oxidation. Such Ni-implanted CoO NP assemblies manifest improved photochemical properties and demonstrate good possibilities for widespread uses in photocatalysis and environmental remediation.

4. Experimental

4.1 Synthesis of $Co_{1-x}Ni_xO$ NPs

$Co_{1-x}Ni_xO$ (x = 0, 0.01, 0.02 and 0.05) NPs were prepared according to a modified literature procedure.[20] For a typical synthesis of $Co_{0.98}Ni_{0.02}O$ NPs, 1.47 mmol of $Co(acac)_3$ (98%, Sigma-Aldrich), 0.03 mmol of $Ni(NO_3)_2{\cdot}6H_2O$ (98%, Alfa Aesar) and 300 mmol of oleylamine (70%, Sigma-Aldrich) were heated at 135 °C under an inert atmosphere for 5 h. The resulting brown solution was then slowly heated to 200 °C with a heating rate of ~2 °C min^{-1} and maintained at this temperature for 3 h, giving a brown suspension. Next, the supernatant was removed by centrifugation, retrieving the $Co_{0.98}Ni_{0.02}O$ NPs in a powdery form. The $Co_{0.98}Ni_{0.02}O$ NPs were then dispersed in hexane (95%, Sigma-Aldrich) to form a stable colloidal solution (10 mg mL^{-1}). A similar procedure was followed for the synthesis of 1% and 5% Ni-doped CoO NPs, utilizing 1.485 mmol and 0.015 mmol and 1.425 mmol and 0.075 mmol of $Co(acac)_3$ and $Ni(NO_3)_2{\cdot}6H_2O$, respectively.

4.2 Ligand exchange of $Co_{1-x}Ni_xO$ NPs

A dispersion of $Co_{1-x}Ni_xO$ NPs in hexane (6 mL) was added to a solution of $NOBF_4$ (60 mg, 97%, Acros Organics) in DMF (6 mL, 99.9%, Sigma-Aldrich) and the mixture was stirred at room temperature until the NPs were transferred to the DMF phase. The BF_4^--capped $Co_{1-x}Ni_xO$ NPs were then collected by precipitation with toluene (99.7%, Sigma-Aldrich), followed by centrifugation. The ligand-stripped $Co_{1-x}Ni_xO$ NPs were dispersed in DMF to form a stable colloidal solution of 120 mg mL^{-1}.

4.3 Synthesis of $Co_{1-x}Ni_xO$ NP assemblies

Mesoporous $Co_{1-x}Ni_xO$ nanoparticle assemblies (MNAs) were prepared following a previously reported procedure with some modifications.[6] For a typical synthesis of mesoporous $Co_{1-x}Ni_xO$ nanoparticle assemblies (MNAs), 0.2 g of block copolymer Pluronic F127 $(OH(CH_2CH_2O)_{100}(CH(CH_3)CH_2O)_{64}(CH_2CH_2O)_{100}H$, M_n ~12 000, Sigma-Aldrich) were dissolved in 1.5 mL of tetrahydrofuran (THF, >99%, Sigma-Aldrich) with continuous stirring. To this solution, 0.5 mL of colloidal $Co_{1-x}Ni_xO$ NP solution in DMF was added dropwise and the mixture was stirred at room temperature for 2 h. Then, the resulting mixture was placed in an oven at 40 °C and left for 5 days to give a mesostructured $Co_{1-x}Ni_xO$/polymer composite. The resulting dry powder was subsequently heated to 350 °C for 4 h under N_2 flow (*ca.* 50 cm^3 min^{-1}), using a heating rate of 1 °C min^{-1}, to yield the mesoporous product.

4.4 Photocatalytic reactions

In a typical procedure, a quantity of catalyst (10–20 mg) was dispersed in 50 ml of 50 mg L^{-1} Cr(VI) aqueous solution, which were prepared by dissolving $K_2Cr_2O_7$ in deionized (DI) water. The solution pH was adjusted with dilute sulfuric acid. Before irradiation, the suspension was magnetically stirred in the dark for 30 min to ensure adsorption/desorption equilibrium. The photoreduction reaction was performed by irradiating the solution with UV–visible or visible light, using a 300 W Xe lamp (Variac Cermax) with cut-off filters allowing λ >360 nm or λ >420 nm, respectively. All the experiments were carried out at 20 ± 2 °C using a water bath cooling system. During reaction, the concentration of Cr(VI) in the solution was monitored *via* the 1,5-diphenylcarbazide (DPC) colorimetric method, using a PerkinElmer Lambda 25 UV–vis spectrometer. Control experiments were carried out with the addition of phenol, citric acid and EDTA (1 equiv.) into the reaction mixture.

For the photooxidation of water to oxygen, 15 mg of the $Co_{0.98}Ni_{0.02}O$ MNA catalyst and 50 mL of 50 mg L^{-1} Cr(VI) aqueous solution (pH = 2) were placed into a 100 mL airtight quartz tube. The temperature of the suspension was maintained at 20 ± 2 °C by using an external water-cooling system. The mixture was first purged with argon for 30 min under atmospheric pressure to remove any dissolved air and then irradiated with a 300 W Xe lamp (λ >360 nm). The O_2 generated from the reaction was analyzed with a gas chromatograph (Shimadzu GC-2014) equipped with a thermal conductivity detector.

The O_2 evolution transient experiments were performed under λ >360 nm light irradiation in an air-tight quartz cell containing 0.3 g L^{-1} $Co_{0.98}Ni_{0.02}O$ MNA catalyst and 50 mg L^{-1} Cr(VI) aqueous solution (pH = 2) and the evolved gas was monitored with an on-line gas analyzer (Hiden HPR-20 QIC).

The apparent quantum yield (QY) of the catalyst was calculated by analyzing the amount of reduced Cr(VI) at given monochromatic irradiation, using LED light with wavelengths of 375 and 410 nm, respectively:

$$\mathrm{QY} = \frac{3 \times \text{number of reduced Cr(VI)}}{\text{number of incident photons}} \quad (2)$$

The flux of incident photons was measured using a StarLite energy meter equipped with a FL400A-BB-50 fan-cooled thermal sensor (Ophir Optronics Ltd, Jerusalem).

4.5 Physical characterization

Thermogravimetric analysis was performed on a PerkinElmer Diamond instrument under a N_2 atmosphere (~200 mL min^{-1}

flow rate) with a heating rate of 5 °C min^{-1}. Powder X-ray diffraction (XRD) patterns were collected on a PANalytical X'Pert Pro X-ray diffractometer (45 kV and 40 mA) using Cu Kα (λ = 1.5418 Å) radiation (45 kV, 40 mA). XRD data were recorded in the 2θ range of 30–80° with a 2θ step size of 0.01° and a scanning speed of 0.1° min^{-1} in Bragg–Brentano geometry. Elemental microprobe analyses were performed by using a JEOL JSM-6390LV scanning electron microscope (SEM) equipped with an Oxford INCA PentaFETx3 energy-dispersive X-ray spectroscopy (EDS) detector (Oxfordshire, UK). Data acquisition was performed at least five times for each sample using an accelerating voltage of 20 kV and a 100 s accumulation time. Anodic stripping voltammetry (ASV) was performed using a trace metal analyzer (797 VA Computrace, Metrohm AG Ltd, Switzerland). A three-electrode system was used comprising a hanging mercury drop electrode (HMDE) as the working electrode, platinum (Pt) as the auxiliary electrode and Ag/AgCl (3 M KCl) as the reference electrode. Before analysis, the Ni-doped CoO samples were dissolved in 5 mL aqua regia and the solutions were diluted appropriately, so that the measuring concentrations were less than 10 ppb. The analysis has been conducted following the AN-V-87 protocol developed by Metrohm.[21] X-ray photoelectron spectroscopy (XPS) measurements were carried out using a monmonochromatic Mg K_α line at 1253.6 eV (12 kV with 20 mA anode current) and a Leybold LH EA11 electron energy analyzer operated at a constant pass energy of 100 eV. The analyzed area was a 1.5 × 5 mm^2 rectangle, placed near the center of the powder-covered area on each specimen surface. In all XPS spectra, the binding energy of the predominant aliphatic contribution to the C 1s peak at 284.8 eV was used as a reference. Transmission electron microscopy (TEM) images were taken with a JEOL JEM-2100 electron microscope equipped with a LaB_6 filament and operated at 200 kV accelerating voltage. Samples were prepared by suspending fine powders in anhydrous ethanol and then drop casting on a copper grid covered with a carbon film. Nitrogen adsorption–desorption isotherms were measured at −196 °C on a Quantachrome NOVA 3200*e* sorption analyzer. Before measurement, samples were degassed at 100 °C under vacuum (<10^{-5} Torr) for at least 12 h. The specific surface areas were calculated using the Brunauer–Emmett–Teller (BET) method on the adsorption data in the relative pressure range of 0.05–0.22. The total pore volumes were estimated from the adsorbed amount at the relative pressure (P/P_0) of 0.98, and the pore size distributions were obtained from the adsorption branch of the isotherms, using the non-local density functional theory (NLDFT) method.[22] UV–vis diffuse reflectance spectra were recorded with a PerkinElmer Lambda 950 optical spectrophotometer, using $BaSO_4$ powder as a 100% reflectance standard. Diffuse reflectance data were converted to absorption using the Kubelka–Munk function $F = (1 - R)^2/(2R)$, where R is the measured reflectance.[23] Fluorescence spectra were obtained at room temperature on a Lumina Fluorescence spectrometer (Thermo scientific) equipped with a 150 W Xe lamp.

4.6 Electrochemical measurements

Mott–Schottky measurements were performed in a 0.5 M Na_2SO_4 aqueous electrolyte (pH = 7) using a Metrohm Autolab PGSTAT 302N potentiostat. A three-electrode set-up, with a platinum plate (1.0 × 2.0 cm^2) and a silver–silver chloride (Ag/AgCl, 3 M KCl) as the counter and reference electrodes, respectively, was adopted to study the samples. The capacitance of the semiconductor/electrolyte interface was obtained at 1 kHz, with 10 mV AC voltage amplitude.

For the semiconductor–electrolyte interface, the capacitance C_{sc} of the space charge region can be described as follows:

$$\frac{1}{{C_{sc}}^2} = \frac{2(E - E_{FB})}{\varepsilon\varepsilon_o A q_e N_A} \quad (3)$$

where C_{sc} is the space charge capacitance, E is the applied potential, E_{FB} is the flat-band potential, N_A is the carrier density of the electrode material, ε is the relative dielectric constant of CoO (13), ε_o is the dielectric permittivity of vacuum (8.8542 × 10^{-10} F cm^{-1}), A is the area of the electrode and q_e is the elementary charge (1.602 × 10^{-19} C).

The carrier density (N_A) of the samples can be calculated using the following equation:

$$N_A = \frac{2(E - E_{FB}) \times {C_{sc}}^2}{\varepsilon\varepsilon_o A q_e} \quad (4)$$

For Nyquist plots, a small AC perturbation of 20 mV was applied to the electrodes, and the different current output was measured throughout a frequency range of 1 to 10^6 Hz. The steady state DC bias was kept at 0 V (open-circuit potential) throughout the EIS experiments. All these experiments were conducted under dark conditions. The measured potential *vs.* the Ag/AgCl reference electrode was converted to the normal hydrogen electrode (NHE) scale using the formula: $E_{NHE} = E_{Ag/AgCl} + 0.210$ V.

The working electrodes for impedance-potential measurements were fabricated as follows: ~10 mg of each sample was dispersed in 1 mL DI water and the mixture was subjected to sonication in a water bath until a uniform suspension was formed. After that, 40 μL of the suspension was drop-cast onto the surface of the fluorine-doped tin oxide (FTO, 9 Ω sq^{-1}) substrate, which was masked with an epoxy resin to expose an effective area of 1.0 × 1.0 cm^2. The sample was dried in a 60 °C oven for 30 minutes.

4.7 Photoelectrochemical measurements

Photoelectrochemical measurements were carried out in an air-tight three-electrode cell with the samples as the working electrode (1 cm^2 illumination area), Ag/AgCl (3 M KCl) as the reference electrode, and a platinum wire as the counter electrode. Photocurrent data were collected at a potential of 1 V (*vs.* Ag/AgCl) in 0.5 M KOH aqueous electrolyte. Before analysis, the electrolyte was purged with N_2 for 30 min to remove the oxygen. The photocurrent densities of the samples were measured using a Metrohm Autolab PGSTAT 302N potentiostat coupled with a neutral white light-emitting diode (WLED, λ = 420–760 nm).

4.8 Theoretical calculations

Density functional theory (DFT) calculations were performed using the Vienna *ab initio* Simulation Package (VASP).[24] The projector augmented wave method (PAW) for the core electrons and the nuclei was used.[25] For the exchange–correlation functional, we tested both the local density approximation (LDA)[26] and the generalized gradient approximation (GGA) of Perdew–Burke–Ernzerhof (PBE).[27] We found that LDA describes the electronic structure of CoO as a semiconductor better than GGA-PBE, in agreement with previous studies[28] and results reported here are from LDA calculations only. In order to account for the on-site repulsion between d electrons, DFT+U within Dudarev's approach was adopted with *U–J* parameter values of 4 and 7 for Co and Ni, respectively.[29] Wave functions were expanded on a plane wave basis set with a 512 eV kinetic energy cutoff and, in the results for the electronic density of states presented here, a 6 × 6 × 6 *k*-point BZ sampling was employed. The ground state was in the antiferromagnetic (AFM) configuration. Simulation cells of several sizes were used (with a minimum of four atoms) in order to examine doping in bulk CoO with different Ni concentrations.

Conflicts of interest

There are no conflicts to declare.

Acknowledgements

We gratefully acknowledge financial support from the Special Account for Research Funds of the University of Crete (SARF UOC) (KA 10138).

Notes and references

1 P. Miretzky and A. F. Cirelli, *J. Hazard. Mater.*, 2010, **180**, 1.
2 L. Levankumar, V. Muthukumaran and M. B. Gobinath, *J. Hazard. Mater.*, 2009, **161**, 709.
3 D. Wang, Y. Ye, H. Liu, H. Ma and W. Zhang, *Chemosphere*, 2018, **193**, 42.
4 (*a*) C. Mondal, M. Ganguly, J. Pal, A. Roy, J. Jana and T. Pal, *Langmuir*, 2014, **30**, 4157; (*b*) X. Liu, L. Pan, T. Lv, G. Zhu, Z. Suna and C. Sun, *Chem. Commun.*, 2011, **47**, 11984; (*c*) L. Yang, Y. Xiao, S. Liu, Y. Li, Q. Cai, S. Luo and G. Zeng, *Appl. Catal., B*, 2010, **94**, 142; (*d*) J. Yu, S. Zhuang, X. Xu, W. Zhu, B. Feng and J. Hu, *J. Mater. Chem. A*, 2012, **3**, 1199; (*e*) G. Odling, A. Ivaturi, E. Chatzisymeon and N. Robertson, *ChemCatChem*, 2017, **10**, 234; (*f*) C. Yu, P. Yang, L. Tie, S. Yang, S. Dong, J. Sun and J. Sun, *Appl. Surf. Sci.*, 2018, **455**, 8.
5 (*a*) Z.-J. Jiang and Z. Jiang, *Sci. Rep.*, 2016, **6**, 27081; (*b*) K. M. Nam, W. S. Seo, H. Song and J. T. Park, *NPG Asia Mater.*, 2017, **9**, e364.
6 G. Velegraki, J. Miao, C. Drivas, B. Liu, S. Kennou and G. S. Armatas, *Appl. Catal., B*, 2018, **221**, 635.
7 (*a*) D. Gu, C.-J. Jia, C. Weidenthaler, H.-J. Bongard, B. Spliethoff, W. Schmidt and F. Schüeth, *J. Am. Chem. Soc.*, 2015, **137**, 11418; (*b*) Z. Mao, J. Chen, Y. Yang, D. Wang, L. Bie and B. D. Fahlman, *ACS Appl. Mater. Interfaces*, 2017, **9**, 12427; (*c*) L. Liao, Q. Zhang, Z. Su, Z. Zhao, Y. Wang, Y. Li, X. Lu, D. Wei, G. Feng, Q. Yu, X. Cai, J. Zhao, Z. Ren, H. Fang, F. R. Hernandez, S. Baldelli and J. Bao, *Nat. Nanotechnol.*, 2014, **9**, 69.
8 (*a*) I. T. Papadas, I. Vamvasakis, I. Tamiolakis and G. S. Armatas, *Chem. Mater.*, 2016, **28**, 2886; (*b*) I. T. Papadas, S. Fountoulaki, I. N. Lykakis and G. S. Armatas, *Chem. – Eur. J.*, 2016, **22**, 4600.
9 F. Rouquerol, J. Rouquerol and K. S. W. Sing, *Adsorption by Powders and Porous Solids: Principles, Methodology and Applications*, Academic Press, London, 1999.
10 (*a*) S. Wang, M. Chen, Y. Xie, Y. Fan, D. Wang, J. J. Jiang, Y. Li, H. Grutzmacher and C. Y. Su, *Small*, 2016, **12**, 2365; (*b*) J. S. Gwag and Y. Sohn, *Bull. Korean Chem. Soc.*, 2012, **33**, 505.
11 J. F. Marco, J. R. Gancedo, M. Gracia, J. L. Gautier, E. I. Rios, H. M. Palmer, C. Greaves and F. J. Berry, *J. Mater. Chem.*, 2001, **11**, 3087.
12 S. Zhao, Y. Wang, J. Dong, C.-T. He, H. Yin, P. An, K. Zhao, X. Zhang, C. Gao, L. Zhang, J. Lv, J. Wang, J. Zhang, A. M. Khattak, N. A. Khan, Z. Wei, J. Zhang, S. Liu, H. Zhao and Z. Tang, *Nat. Energy*, 2016, **1**, 16184.
13 H.-K. Lin, H.-C. Chiu, H.-C. Tsai, S.-H. Chien and C.-B. Wang, *Catal. Lett.*, 2003, **88**, 169.
14 A. Tanaka, K. Nakanishi, R. Hamada, K. Hashimoto and H. Kominami, *ACS Catal.*, 2013, **3**, 1886.
15 N. Nasrallah, M. Kebir, Z. Koudri and M. Trari, *J. Hazard. Mater.*, 2011, **185**, 1398.
16 R. Gherbia, N. Nasrallaha, A. Amraneb, R. Maachia and M. Trari, *J. Hazard. Mater.*, 2011, **186**, 1124.
17 A. Zhitkovich, *Chem. Res. Toxicol.*, 2005, **18**, 3.
18 (*a*) Z. B. Alfassi, R. E. Huie, S. Marguet, E. Natarajan and P. Neta, *Int. J. Chem. Kinet.*, 1995, **27**, 181; (*b*) J. Colucci, V. Montalvo, R. Hernandez and C. Poullet, *Electrochim. Acta*, 1999, **44**, 2507; (*c*) A.-M. Manke, K. Geisel, A. Fetzer and P. Kurz, *Phys. Chem. Chem. Phys.*, 2014, **16**, 12029.
19 (*a*) J. Bisquert, H. Randriamahazaka and G. Garcia-Belmonte, *Electrochim. Acta*, 2005, **51**, 627; (*b*) L. M. Da Silva, K. C. Fernandes, L. A. De Faria and J. F. Boodts, *Electrochim. Acta*, 2004, **49**, 4893.
20 W. S. Seo, J. H. Shim, S. J. Oh, E. K. Lee, N. H. Hur and J. T. Park, *J. Am. Chem. Soc.*, 2005, **127**, 6188.
21 http://www.metrohm.com/en/applications/#.
22 P. I. Ravikovitch, D. Wei, W. T. Chueh, G. L. Haller and A. V. Neimark, *J. Phys. Chem. B*, 1997, **101**, 3671.
23 P. Kubelka, *J. Opt. Soc. Am.*, 1948, **38**, 448.
24 (*a*) G. Kresse and J. Hafner, *Phys. Rev. B: Condens. Matter Mater. Phys.*, 1993, **47**, 558; (*b*) G. Kresse and J. Furthmüller, *Comput. Mater. Sci.*, 1996, **6**, 15; (*c*) G. Kresse and J. Furthmüller, *Phys. Rev. B: Condens. Matter Mater. Phys.*, 1996, **54**, 11169.

25 (*a*) P. E. Blöchl, *Phys. Rev. B: Condens. Matter Mater. Phys.*, 1994, **50**, 17953; (*b*) P. E. Blöchl, O. Jepsen and O. K. Andersen, *Phys. Rev. B: Condens. Matter Mater. Phys.*, 1994, **49**, 16223; (*c*) G. Kresse and D. Joubert, *Phys. Rev. B: Condens. Matter Mater. Phys.*, 1999, **59**, 1758.
26 J. P. Perdew and A. Zunger, *Phys. Rev. B: Condens. Matter Mater. Phys.*, 1981, **23**, 5048.
27 J. P. Perdew, K. Burke and M. Ernzerhof, *Phys. Rev. Lett.*, 1996, **77**, 3865.
28 N. Alidoust, M. Lessio and E. A. Carter, *J. Appl. Phys.*, 2016, **119**, 025102.
29 S. L. Dudarev, G. A. Botton, S. Y. Savrasov, C. J. Humphreys and A. P. Sutton, *Phys. Rev. B: Condens. Matter Mater. Phys.*, 1998, **57**, 1505.